AFRL-RV-PS-
TR-2013-0150
AFRL-RV-PS-
TR-2013-0150

PHYSICS OF SOLAR FLARES AND DEVELOPMENT OF STATISTICAL AND DATA DRIVEN MODELS

K. S. Balasubramaniam, et al.

30 September 2013

Final Report

AIR FORCE RESEARCH LABORATORY
Space Vehicles Directorate
3550 Aberdeen Ave SE
AIR FORCE MATERIEL COMMAND
KIRTLAND AIR FORCE BASE, NM 87117-5776

DTIC COPY

NOTICE AND SIGNATURE PAGE

AFRL-RV-PS-TR-2013-0150 HAS BEEN REVIEWED AND IS APPROVED FOR PUBLICATION IN ACCORDANCE WITH ASSIGNED DISTRIBUTION STATEMENT.

//SIGNED//	//SIGNED//
Dr. Karatholuvu Balasubramaniam Program Manager/RVBXS	Edward J. Masterson, Colonel, USAF Chief, Battlespace Environment Division

REPORT DOCUMENTATION PAGE

Form Approved
OMB No. 0704-0188

1. REPORT DATE *(DD-MM-YYYY)*	**2. REPORT TYPE**	**3. DATES COVERED** *(From - To)*
30-09-2013	Final Report	15 Jun 2010 – 30 Sep 2013

4. TITLE AND SUBTITLE
Physics of Solar Flares and Development of Statistical and Data Driven Models

5a. CONTRACT NUMBER

5b. GRANT NUMBER

5c. PROGRAM ELEMENT NUMBER
62601F

6. AUTHOR(S)
K. S. Balasubramaniam, D. C. Norquist, T. Henry, and M. Kirk

5d. PROJECT NUMBER
3001

5e. TASK NUMBER
PPM00000587

5f. WORK UNIT NUMBER
EF004376

7. PERFORMING ORGANIZATION NAME(S) AND ADDRESS(ES)
Air Force Research Laboratory
Space Vehicles Directorate
3550 Aberdeen Avenue SE
Kirtland AFB, NM 87117-5776

8. PERFORMING ORGANIZATION REPORT NUMBER
AFRL-RV-PS-TR-2013-0150

9. SPONSORING / MONITORING AGENCY NAME(S) AND ADDRESS(ES)

10. SPONSOR/MONITOR'S ACRONYM(S)
AFRL/RVBXS

11. SPONSOR/MONITOR'S REPORT NUMBER(S)

12. DISTRIBUTION / AVAILABILITY STATEMENT
Approved for Public Release; distribution is unlimited. (377ABW-2013-0975 dtd 06 Nov 2013)

13. SUPPLEMENTARY NOTES

14. ABSTRACT
Solar flares impact DoD and civilian space- and ground-based assets. The current state of predictability of solar flares, such as the probability of a solar flare occurring (NOAA Space Weather Prediction Center, and USAF/AFWA) are evaluated based on once-a-day measurement and resultant change of solar activity parameters, such as sunspot magnetic classification. With the advent of the USAF's prototype Improved Solar Observing Optical Network telescope, we have the capability to monitor rapid changes in characteristics of the solar chromosphere (1-minute cadence), photosphere (5-minute cadence) and corona (10-minute cadence). We will also use the GOES x-ray data (1-minute cadence) and other space data to complement these measurements. These data sources of past and current data will help us research, track and establish the relationship between the high-cadence variation of measured parameters at the various layers (sunspot umbral and penumbral areas, plage index, magnetic flux, sequential chromospheric brightenings, development of flare ribbons, etc.) and solar flares. We will research the seemingly heterogeneous and voluminous parameterized observational data to understand the measures needed for flare forecasts, incorporating such techniques as principal component analysis, discriminant analysis, genetic algorithms and neural networks. The goal is to demonstrate parameters that could be used in real-time operations to predict the near-term probability of flare occurrence. This research will help gain insights into physical mechanisms of the flaring proF298cess. It will aid in the development of physics-based solar flare forecast models. This report provides the final summary of the work performed under this AFOSR task. Individual and interim technical work has been published in peer-reviewed journals and presented in professional society meetings as appropriate.

15. SUBJECT TERMS
Solar atmosphere, eruptions, flares, chromosphere, filaments, solar magnetic fields, image processing, spectroscopy

16. SECURITY CLASSIFICATION OF:			**17. LIMITATION OF ABSTRACT**	**18. NUMBER OF PAGES**	**19a. NAME OF RESPONSIBLE PERSON**
a. REPORT	**b. ABSTRACT**	**c. THIS PAGE**			Dr. Karatholuvu Balasubramaniam
Unclassified	Unclassified	Unclassified	Unlimited	26	**19b. TELEPHONE NUMBER** *(include area code)*

This page is intentionally left blank.

Table of Contents

List of Figures

Acknowledgements

This work was supported and funded by the Air Force Office of Scientific Research (AFOSR). This report provides the final summary of the work performed under this AFOSR task. Individual and interim technical work has been published in peer-reviewed journals and presented in professional society meetings as appropriate. This final report and relevant research was supported by technical collaborators: D. C. Norquist (Co-PI), T. Henry, and M. Kirk, and R. Hock. We express gratitude to the National Solar Observatory, Air Force Research Laboratories, and numerous individuals from these organizations. Data sources for the work described elsewhere in individual research papers include the National Solar Observatory, NASA/SOlar and Heliophysics Observatory (SOHO), NASA/Solar Dynamics Observatory (SOHO), and are acknowledged in the appropriate individual publications, as appropriate. The Interactive Data Language (IDL) was used for much of the analysis in this study.

We thank Dr. Richard Radick for his encouragement, help and support in executing this effort.

This page is intentionally left blank.

1. INTRODUCTION

Solar flares [1, 2]* are a significant source of violent space weather (see e.g. reviews in [3, 4]*). Alternatively, a solar flare can perhaps be defined as a homogeneous entity that exhibits predefined behavior in the real world and is composed of heterogeneous parts that do not individually exhibit that behavior. It may be thought of as an integrated configuration of components and/or subsystems (in a system engineering sense) – except that the system cannot be actively probed but has to be passively observed. This encapsulates the realm of challenges that face solar flare prediction.

Some good research on understanding the individual variations of solar activity, including sunspot number counts and sunspot magnetic class [5, 6]*, have formed the basis for current flare prediction techniques used by the NOAA Space Weather Prediction Center (SWPC) and the Air Force Weather Agency (AFWA). However, the current operational probabilistic forecast models use solar variations over a cadence of only once-a-day. More advanced research into variations of solar activity parameters such as active region monitoring (see e.g. [7-9]*) and magnetic fields [10-15]* have been performed leading to more recently posed flare prediction schemes. However, consistent availability of high quality and high cadence measurements of the Sun's photosphere and chromospheres have been lacking until recently. In December 2002 the AFRL prototype Improved Solar Observing Optical Network (ISOON) telescope [16]* began to make such measurements at the National Solar Observatory (NSO), Sacramento Peak.

With availability of high photometric quality ISOON data (1-minute cadence chromospheric imaging; 5-minute cadence photospheric continuum imaging) coupled with the availability of NSO Global Oscillations Network Group (GONG) magnetograms (at 1-minute cadence), and similar ground and space-based data (SOHO: Solar and Heliophysics Observatory; SDO: Solar Dynamics Observatory), it is now possible to quantitatively parameterize and track solar features on a minute-by-minute basis. Such fluctuations in physical quantities, before and after flares include: sunspot umbral and penumbral areas, their intensity and area oscillations, sunspot magnetic fields, chromospheric plage areas, filament eruption characteristics, flare nimbus areas and other phenomenological properties thought to be associated with flare activity. The research objectives of this work are to:

(a) To determine consistent relationships between solar flares and measured physical parameters at the solar photosphere, chromosphere and corona, at high cadence, and to develop automatic characterization of time-series imagery data using tools such as Principal Component Analysis (PCA).

(b) To explore tools and techniques needed for solar flare prediction using machine learning algorithms tools such as regression analysis, multivariate discriminant analysis, genetic algorithms, and/or neural networks. The inputs to these models will be derived from objective 1.

.

2. BACKGROUND

2.1. Sunspot Area Data Analysis – Solar Flares Influence

Solar flares are mostly seen in active regions containing sunspots. Sunspots represent the strongest magnetic fields, with the sunspot umbra carrying the strongest and mostly vertical field to the local solar normal about which the sunspot is located, the penumbra carrying the inclined fields from near vertical to near horizontal. The expectation is that the sheared magnetic energy will lead to a modification of the vertical and horizontal components of the magnetic field and thereby the resulting umbral and penumbral areas before and after solar flares have erupted [17]* Along similar lines, this study uses the individual photometric imaging data from the ISOON; Figure 1) to examine measured, detailed features of sunspot groups, such as the penumbral areas and radiation blocking, and their relationship to flares. Such models can be used for predicting solar flares.

2.2. Sequential Chromospheric Brightenings (SCB) Analysis

SCB's are a spatially apparent, temporally connected set of sequential chromospheric brightenings observed in the narrow spectral band (80-100 mA) cores of the Hα spectral line[18]*. They occur in areas surrounding large flares that accompany filament eruptions, a significant number of them accompanying CMEs. [19]* . The sequential nature of the brightenings give the appearance of a wave-like disturbance accompanying flares. In identifying large eruptive flares, it is important to separate out local brightenings versus flare cores to understanding the underlying physics of the large eruptions. This will help us construct better models of solar flares and CMEs. To understand SCBs, this work was to track, identify and classify SCBs and their relationship to flare kernels. Since SCBs occur in large flares accompanying CMEs, and they are detected earlier (20-minutes to an hour) before the CMEs are detected by coronals, tracking SCBs in relationship to flares will help in early identification of CMEs accompanying flares.

2.3. Principal Component Analysis (PCA) Of Flaring Regions

We attempt a method to understand a parametric evaluation of solar flare occurrence using a method called Principal Component Analysis (PCA) (see references in Eydenberg et. al. 2005 [24]) which is commonly employed in understanding a variety of physical phenomena, used in spectroscopy, facial recognition programs, and other classification methods. PCA is a technique that can be used to extract all of the innate characteristics of images by calculating the eigenvectors and eigenvalues of given image matrix, as the entire image may be represented by using only a few of the eigenvectors. Using this reductionist method, a group of images will show similar if not identical principal characteristics in corresponding eigenvectors. Thus, one can compare eigenvectors from similar but not identical images, and extract the same basic information. We propose to find the characteristics of images of active flaring regions in multiple layers of the sun (Chromosphere, photosphere and magnetograms), in order to understand the differences between eruptive and non-eruptive activity.

2.4. Multivariate Discriminant Analysis (MVDA)

The eigenvectors derived from the PCA analysis serve as independent variables in our effort to understand the behavior of flare probability diagnosis from Hα imagery in solar active regions. The goal is short term flare predictability. In the absence of a physical model of active region, we must use

observations in an effort to understand anticipatory signals that can lead to flares. The goals here are to see if the observations can support objective flare forecasting and how best to use them in a suitable technique for the purpose.

3. METHODS, ASSUMPTIONS, AND PROCEDURES

3.1. Sunspot Area Data Analysis

For the ISOON sunspot area data analysis, Figure 1, shows a representative sunspot from a pure continuum (6300 A) image. The solar images were first normalized for limb-darkening changes. We then used histogram-determined thresholds to determine sunspot umbral and penumbral area. Because the location of the sunspot in a solar image is subject to projection effects of a sphere on to a plane, we had to apply appropriate projects to convert from planar (x-y) coordinates to spherical coordinates to determine the actual area. The resulting sunspot areas are measured in millionths of the solar hemisphere. The intensities of the measured sunspot umbral and penumbral areas are normalized to the quiet sun values, to eliminate fluctuations due to atmospheric seeing. A sample fluctuation of the sunspot umbral and penumbral areas and intensities are show in Figure 1. See Section 4.1 for a discussion and results.

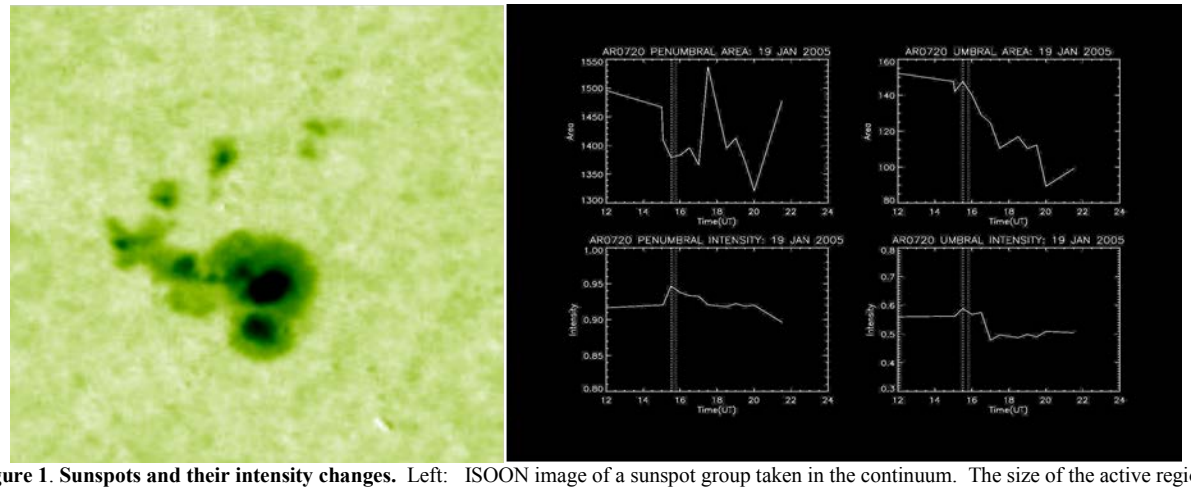

Figure 1. **Sunspots and their intensity changes.** Left: ISOON image of a sunspot group taken in the continuum. The size of the active region shown is: ~170x195 arcseconds. Right: Four panels for intensity fluctuation on 01/19/2005 for NOAA AR10720: top left- penumbral area vs. time; top right- umbral area vs. time; bottom left- penumbral intensity vs. time; bottom right- umbral intensity vs. time. The vertical dotted line represents the start and peak of the flare

3.2. Sequential Chromospheric Brightenings (SCB) Tracking Analysis

This project uses 1.1 arc-second resolution, full-disk, H-α (6563 Å) images taken by the Improved Solar Observing Optical Network (ISOON) telescope at a one minute cadence (Figure 1). To achieve full coverage of the flare's eruption, images from ±3.5 hours from the time of eruption are analyzed yielding approximately 500 images for each event.

Adapting a from Crocker & Weeks algorithm [20]*, the bright kernels of the flare and SCBs are identified and tracked through the duration of the eruption. Image analysis techniques (running difference, Laplacian filter, and morphological transforms) help to identify the flare ribbons and SCBs. These, combined with bright kernel tracking, allow us to differentiate between SCBs and flare ribbons, and extract physical parameters from their evolution. Figure 2 shows the ISOON data used in extracting the position and intensities of SCBs. The ISOON images are 2048 × 2048 pixels with each pixel subtending 1.1 arcseconds. The two-ribbon flaring event shown is from 6 May 2005. Figure 2**A** shows an example of a calibrated Hα ISOON image with the region of

interest (ROI) highlighted. Figure 2B is the region of interest (ROI) after preprocessing. Figure 2C shows the Doppler Image. Figure 2D shows the flare intensity curves over the time period of interest: 12:28 – 22:47 UT. The ISOON Relative curve is an intensity curve normalized to the solar disc center, while the ISOON Peak curve is defined by the maximum value of the ROI in each time step; both curves are normalized. The GOES Soft (1.0 − 8.0 ˚A) and Hard (0.5 − 4.0 ˚A) curves are normalized x-ray intensity curves for reference from the GOES 14 satellite. Figure 3 and 4 shows sample representation of SCB and flare kernels. The SCB intensities and their integrated intensities carry a different profile in both life time, and in their brightness characteristics. Flares last several tens of minutes, while SCBs last only a few minutes, as seen from their full-width at half-maximum (FWHM) curves.

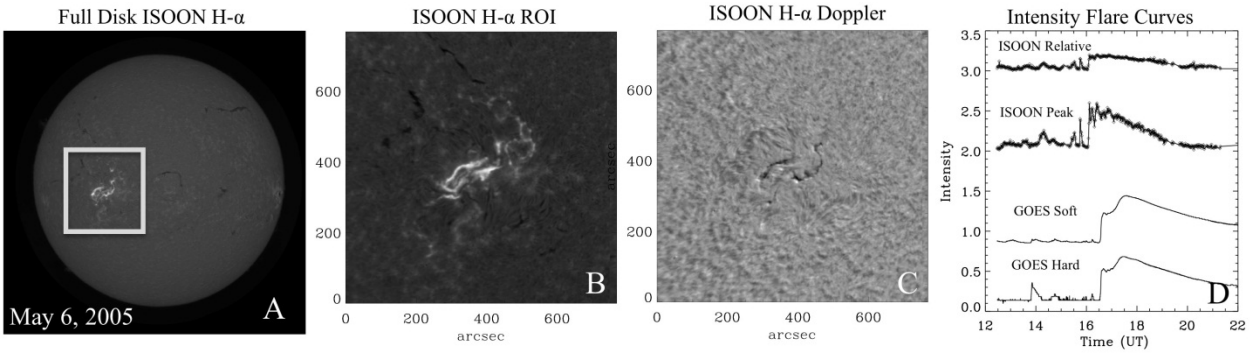

Figure 2. SCBs and their identification. The two-ribbon flaring event from 6 May 2005 is the bright region. See text for details.

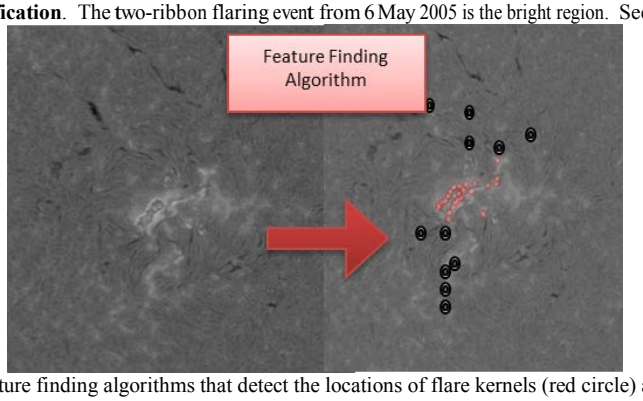

Figure 3. Tracking SCBs. The feature finding algorithms that detect the locations of flare kernels (red circle) and SCB brightenings (white circles) shown, for representation. Not all kernels are shown.

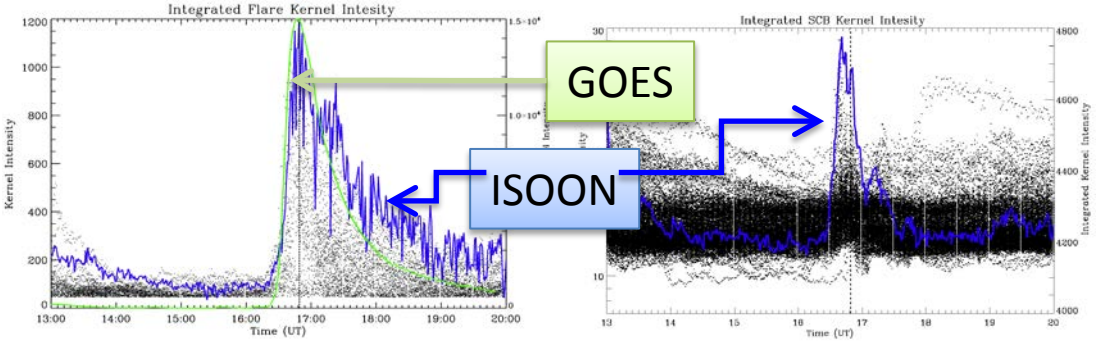

Figure 4. Light Curves of Flares and SCBs. Left: Intensity measures of individual bright kernels and their integrated intensities for flares (with the ISOON and GOES) integrated curves; and Right: for SCBs. Note the integrated intensities and characteristics are different.

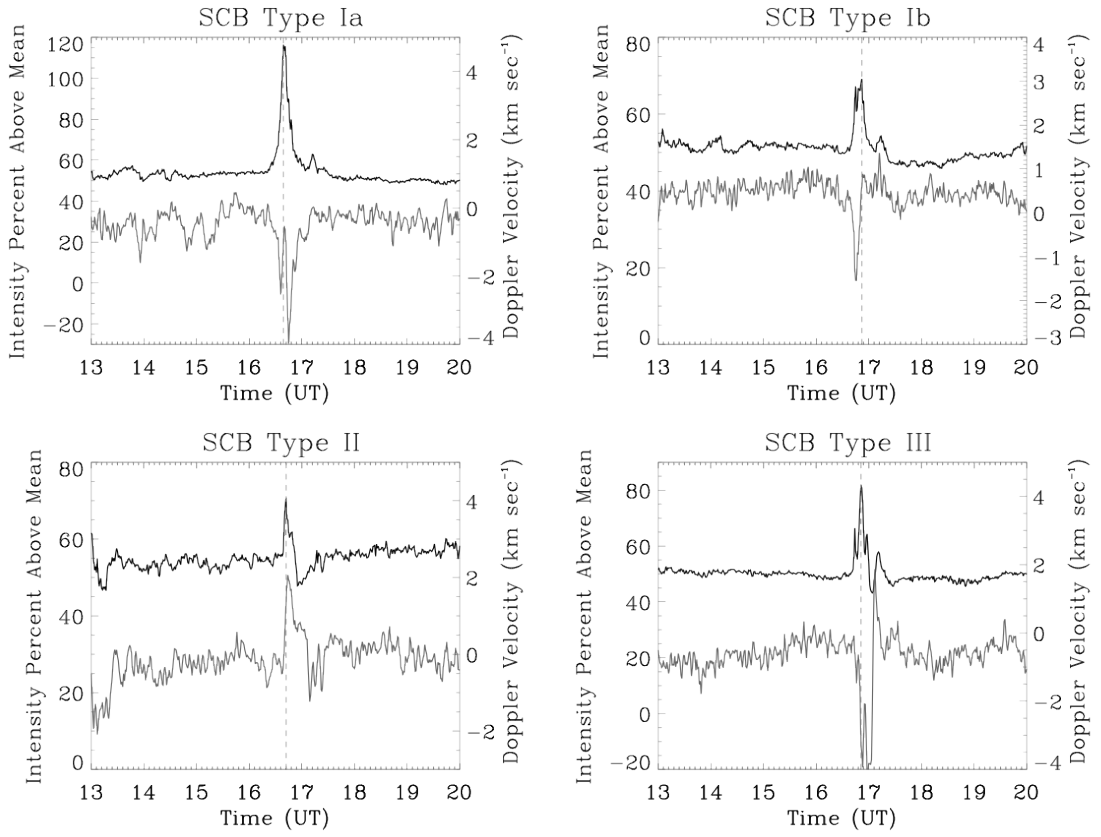

Figure 5: Intensity and Doppler changes in SCBs. Sample intensity and Doppler fluctuations of Type Ia, Ib, II and III SCBs/ The dotted line represent the peak of the solar flare.

Doppler Velocities of SCBs: From a measurement of ISOON Doppler velocity fluctuations we find that SCBs can be made up of four type: Type Ia,b the Doppler velocities are negative while the intensities rise and fall. The subtle difference between 1a and 1b is that while in Ia the Doppler dip succeeds the intensity peak, in Ib the Doppler dip precedes the intensity peak. In type II the Doppler peak is +ve, same as the intensity, and type III where the Doppler and Intensity Peaks are spread and multi-lobed.

3.3. PCA Analysis of Flares

Flares are currently classified simply by the X-ray (GOES 1-8 A) Peak or optical strength. In the PCA analysis, consider a set of measurements *Xi*, where Xi (i=1-n) containing a total number of $n = (x \text{ X } y)$ pixels. The standard deviations, covariance functions, the eigen values and eigenvectors are related to each other, in one-dimension and two-dimensions, respectively, by :

$$s = \sqrt{\frac{\sum_{i=1}^{n}\left(X_i - \overline{X}\right)^2}{n-1}} \qquad s^2 = \frac{\sum_{i=1}^{n}\left(X_i - \overline{X}\right)^2}{n-1} \qquad s^2 = \frac{\sum_{i=1}^{n}\left(X_i - \overline{X}\right)\left(X_i - \overline{X}\right)}{n-1} \tag{1}$$

$$c = \frac{\sum_{i=1}^{n}\left(X_i - \overline{X}\right)\left(Y_i - \overline{Y}\right)}{n-1} \qquad C = \begin{pmatrix} \text{cov}(x,x) & \text{cov}(x,y) \\ \text{cov}(y,x) & \text{cov}(y,y) \end{pmatrix}$$

A solution to the covariance matrix C can be achieved by a single-value decomposition

$$Cw = \lambda w \tag{2}$$

Where w are eigenvectors (the principal components) and λ are the eigen values. The relative strength of the eigen values (λ) decrease with increasing number of principal components. For example a straight line fit (first order polynomial) has only two eigen values, a 2-order polynomical has 3 eigen values, and so on. When one has a sequence of temporally varying images, the two-dimensional image is converted to a one-dimensional spatial stream. The temporal fluctions of each spatial stream then constitutes the second dimension for deriving the covariance matrix. For solar active region, trial and experience tells us that upto about 25 eigen values are useful, and most of the signals are at best embedded within the first 10 eigen values. For example, the temporal variation of the first 9 eigen vectors of a flare are shown in Figure 6.

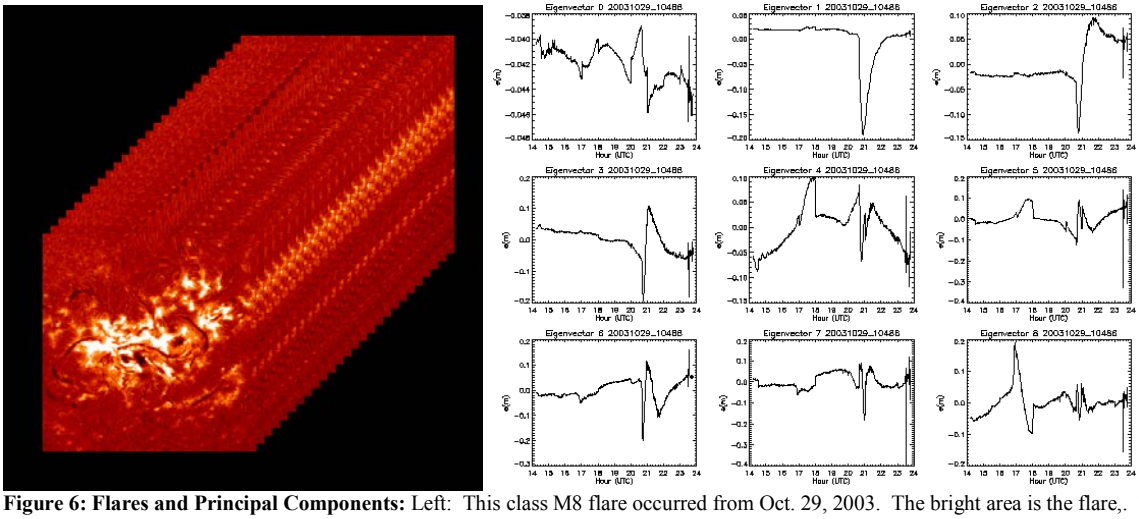

Figure 6: Flares and Principal Components: Left: This class M8 flare occurred from Oct. 29, 2003. The bright area is the flare,. The dark area to the right of the flare is a sunspot. Right: A sample set of 9 eigen vectors for the same flare.

3.4 MVDA Analysis of PCA data

A principal component analysis results in eigen vectors - derived from a sequence of Ha flare images are the starting points - are the inputs to the MVDA. The eigen vectors (an orthogonal set) describe the variables that define a flaring system, The presumption is that the temporal variation of the variables that describe the flaring system have a predictable pattern. The next process is to understand patterns of predictor (the eigen vector) against a predictand (some measureable quantity). The predictand we chose is the GOEx X-ray flare light curve, which is distinctly discernible for these eruptions. The multivariate discriminant algorithm provides a set of discriminant vectors that describe the relationship the predictors and the predictands. The discriminant vectors (discriminants) are determined using a training set of eigen vectors and GOES x-ray light curves

For the present purpose, we truncate the leading eigenvalues explaining 99.9% variance. This results in 25-55 eigenvector that describe the entire signal. The premise of MVDA analysis is the following: For known flares, predictors and predictands hold a discriminant relationship. Eigenvector elements for a time series are the predictors. A specified indicator of flaring is the

predictand. Once discriminant are determined from a known data set (training), the discriminant can then be applied to an unknown data set (testing) to determine probabilities that a predictor signals a flare. Predictor vectors, predictand pairs for all times from selected sequences constituted a "training set". Training set predictors, predictands are used to train MVDA the resulting discriminant vector(s) (DV) applied to predictors to diagnose predictands at image times of interest.

The leading eigen vectors (predictands) for October 29, 2003 are shown in figure 6 (right). Below, figure 7) shows the GOES X-Ray 1-8A data as the predictor.

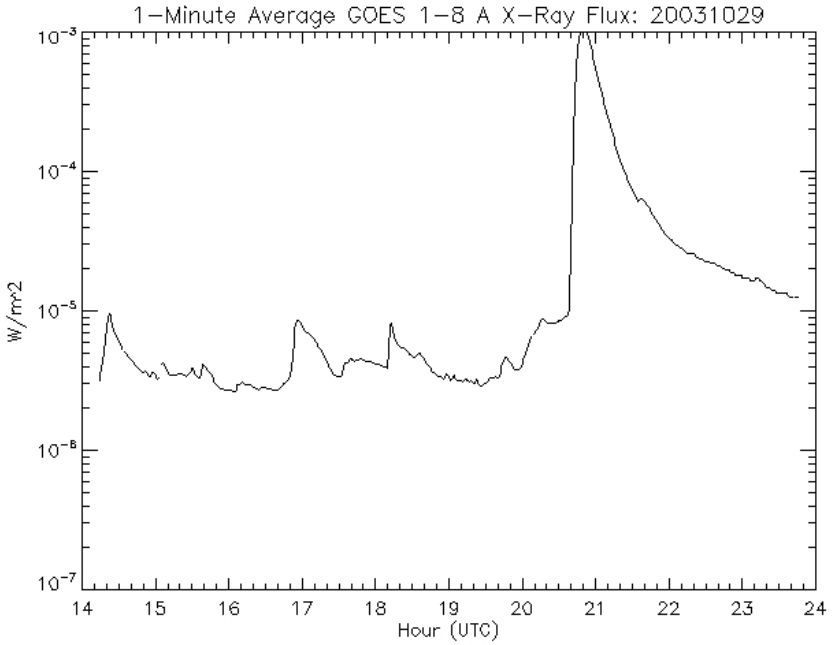

Figure 7: GOES X-Ray Light Curve. This class M8 flare occurred from Oct. 29, 2003. Plot shows the GOES 1-8 X-ray data as the predictor.

Flaring Categories: The flaring data consisted of image sequence of about 90 flaring and non-flaring regions. Based on the a study of all flares in Solar Cycle 23, Norquist [25] found that for a majority (93%) of active region groups no significant flares (x-ray peak > C5) occurred, it was only in a minority of times (~7%) is when flaring occurred. So no-flaring is a genuine flare category. Using the approach of Norquist and Balasubramaniam [26],we divided the flares into 4 flaring categories, called Flare Level Indicators (FLI): FLI = 0 for no flare above x-ray background and smoothly varying (sinusoidal) eigenvectors; FLI = 1 for weak flares (peak flux in the x-ray decade of the background value) with spiked otherwise smoothly varying (sinusoidal) eigenvectors; FLI = 2 for moderate x-ray flares (one decade greater than background) and smoothly curved (non-sinusoidal) eigenvectors before and after the flare spike; FLI = 3 for strong x-ray flares (two or more decades above background) with non-curving eigenvectors before and smoothly curving after sharp spikes. We refer the reader to Norquist and Balasubramaniam [27] for further details on the implementation. The Table 1 below shows three ISOON data sets.

Table 1: List of ISOON Active Regions

ISS 1			ISS 2			ISS 3		
Date	AR #	FLI	Date	AR #	FLI	Date	AR #	FLI
20021213	10213	1	20021213	10215	1	20021213	10220	1
20021213	10223	1	20030102	10234	0	20030102	10239	0
20021213	10224	0	20030117	10254	0	20030117	10255	0
20021219	10229	3	20030117	10257	0	20030117	10259	0
20030117	10250	0	20030117	10258	1	20030203	10274	0
20030117	10256	0	20030203	10272	0	20030206	-----	1
20030117	10260	0	20030318	10318	0	20030318	10319	0
20030203	10276	0	20030331	10321	0	20030331	10324	0
20030318	10323	0	20030331	10326	1	20030401	10318	1
20030331	10323	1	20030401	10321	0	20030401	10325	0
20030331	10325	0	20030401	10323	1	20030509	-----	1
20030401	10319	1	20030513	10358	0	20030516	10357	0
20030401	10326	0	20030522	10362	1	20030528	10365	1
20030516	10356	1	20030605	10373	0	20030605	10375	0
20030528	10368	1	20030606	-----	0	20030606	10377	1
20030604	10373	0	20030606	10375	1	20030610	10375	0
20030606	10373	0	20030610	10380	0	20030611	10375	2
20030609	10375	1	20030611	10375	2	20030611	10377	0
20030610	10377	0	20030612	10375	1	20030612	10380	0
20030611	10380	2	20030612	10377	0	20030613	10380	1
20030611	10381	0	20030613	10377	0	20030616	10380	0
20030612	10381	0	20030620	10385	0	20030620	10387	0
20030616	10385	0	20030623	10386	0	20030623	10387	0
20030620	10386	1	20030623	10397	0	20030624	10386	0
20030620	10388	0	20030624	10387	1	20031031	10488	1
20030623	10388	0	20030625	10391	0	20031104	10486	3
20030624	10390	0	20031029	10486	3	20040105	-----	1
20031104	10486	1	20031104	10486	1	20040316	-----	0
20041007	-----	0	20041109	10696	2	20050506	10758	2
20050513	10759	3	20050909	10808	3	20061206	10930	3

Using these flaring categories, we used the Fisher's Linear Discriminant for two groups (FLDF2G) algorithm (Wilks [28]) to develop the discriminant vector from the predictor vectors and binary predictand categories of a training set of selected sequences.

Testing and training application Sets: Using the ISOON data sets mentioned above, we created predictor-predictand pairs. ie. we combined data from Set 1 and 2 as a test sets where we determined the discriminants and applied it to predict flares from set 3. Similarly, we combined data from Set 2 and 3, determined the discriminants and applied it to predict flares from set 1, and finally determined discriminants from Set 3 and 1 and applied the results to predict flares from Set 2. A summary of the algorithm is presented in Appendix A of Norquist and Balasubramaniam [26]. In Section 4.4, we discuss the results.

4. RESULTS AND DISCUSSION

4.1. Sunspot Area Data Analysis

Using the ISOON continuum intensity data, we measured the trends in properties of 141 flares observed during 2003-2010. The flares are separated into GOES x-ray maximum peaks of B (51) flares, C (62 flares), M (16 flares) and X (5 flares). We measured the following trends in sunspot properties before and after flares. (a) increases in umbral area (ua+), (b) decreases in umbral area (ua-), (c) increases in umbral brightness (ub+) , (d) decreases in umbral brightness (ub-), (e) increases in penumbral area (pa+), (f) decreases in penumbral area (pa-), (g) increases in penumbral brightness (pb+) and (h) decreases in penumbral brightness (pb-). The plots are shown in figure 8.

4.2. Sequential Chromospheric Brightenings

Using automated methods to monitor brightenings can now help us classify as to which brightenings belong to flares, and which sequential brightenings belong to SCBs, based on a their intensity and Doppler characteristics. Early identification of both Doppler (sign, location and amplitude) and relative intensity peaks help us distinguish and early identification between the flares accompanied by CMEs and flares without CMEs. The resulting works on identification, analysis and physics of SCBs have been published [21-23]*

4.3. PCA Analysis Of Flares

We ordered the same principal components (for example principal component # 2) for a number of solar flares from A-X class. A sample set of results are shown in Figure 9. First principal component for 18 flares, peak energies ranging from A6.4 – X 10.9. Notice that flares A6.4 to about B6.6 are similar in shape for the small flares. For flares between M8.5 – X 10.9, a different pattern persists. Flares ranging from C4-C8 have an anomalous behaviour.

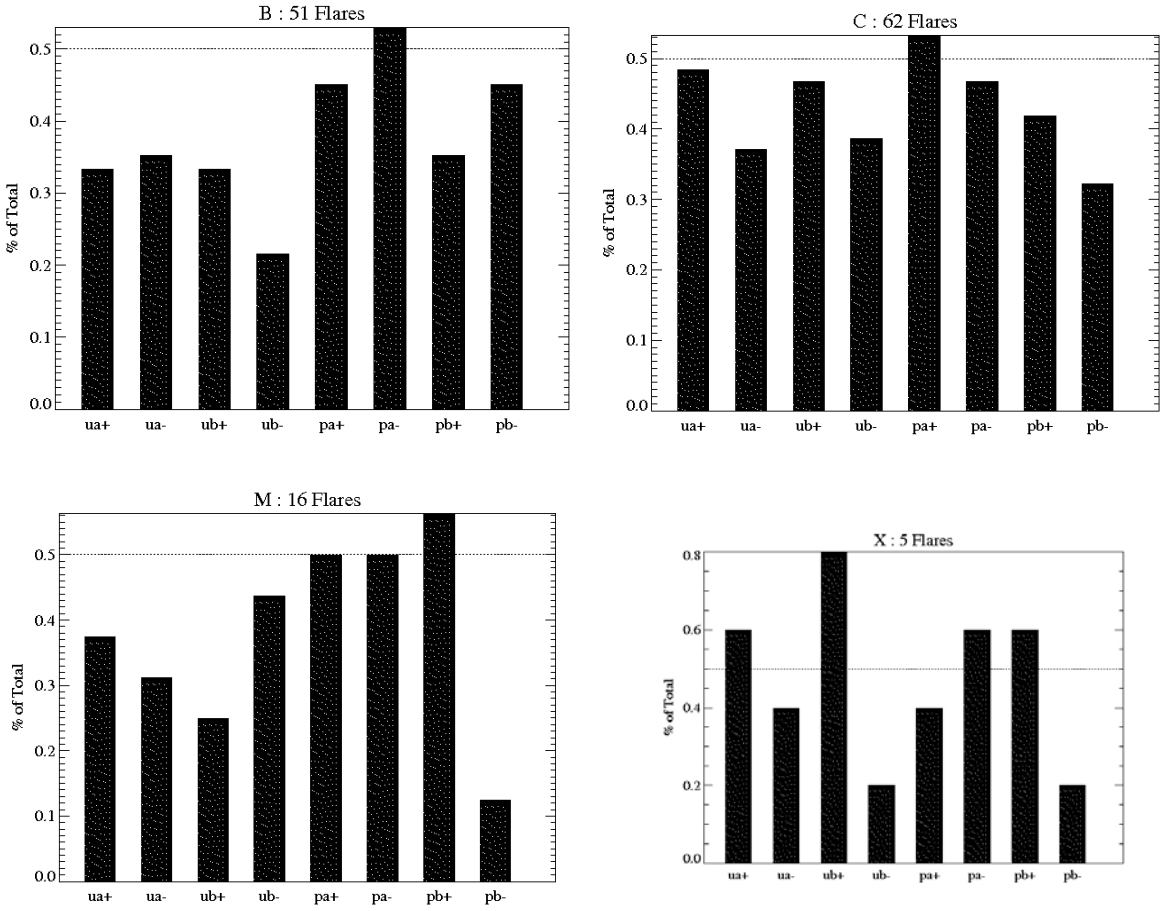

Figure 8: **Frequency of Flares.** Relative increases or decreases in sunspot umbral and penumbral areas, umbral and penumbral intensities before and after flares. See accompanying text for details. The vertical axis is normalized to total unity A trend better than 50% (0.5 on the scale; or significane) shows the reliability of the measurement, for probabilistic use in flare prediction.

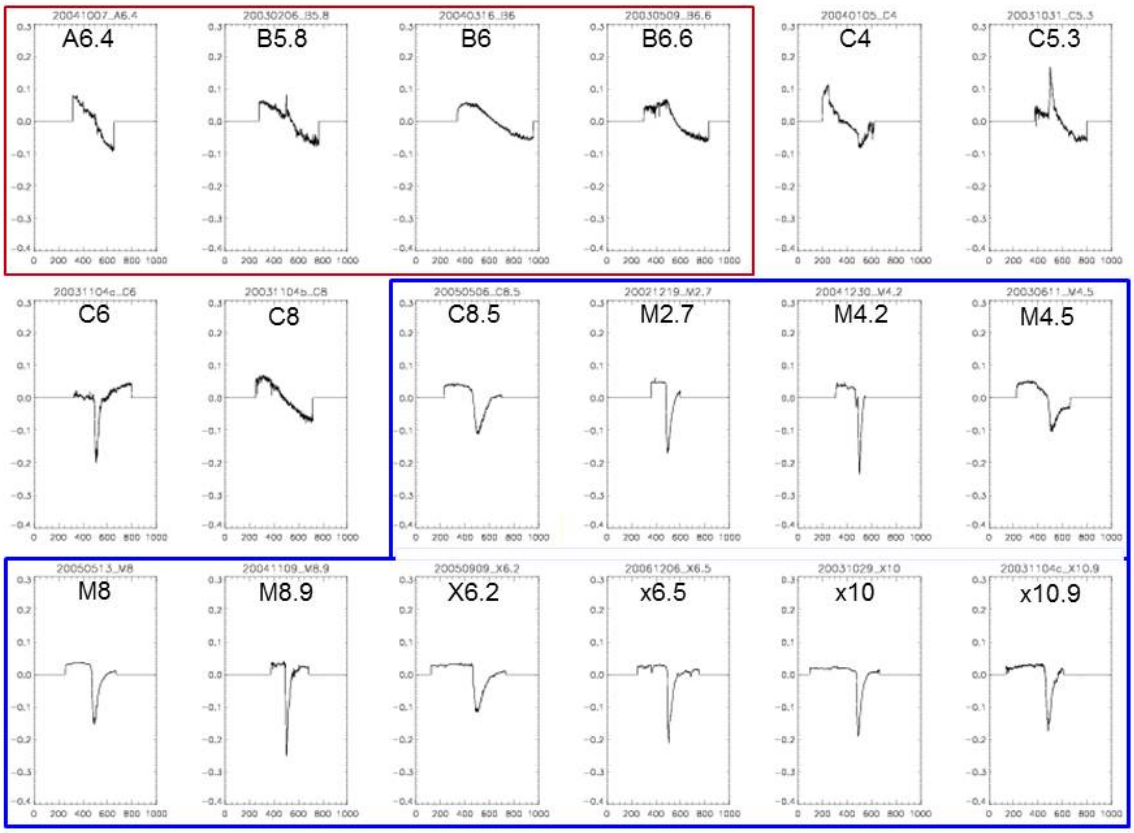

Figure 9: **Patterns of PCA in various flares** : First principal component for 18 flares, peak energies ranging from A6.4 – X 10.9. Notice that flares A6.4 to about B6.6 are similar in shape for the small flares. For flares between M8.5 – X 10.9, a different patterns persists. Flares ranging from C4-C8 have an anomalous behaviour.

4.4. MVDA Analysis Of Flare Categories Results: Summary

Using the MVDA algorithm is presented in Appendix A of Norquist and Balasubramaniam [26], we executed the development algorithm of Image Time Flare Probability Diagnosis Methods 1 and 2 using successive pairs of the three ISOON Image Sequence Sets (ISS) (listed in Table 1 of Norquist and Balasubramaniam [27]). Each ISS have approximately equal number of each of the FLI categories (~ 25 flares for each category; see Sec. 3.4)

We computed a probability-weighted diagnosed flaring category C_p given by

$$C_{p_i} = \sum_{g=0}^{G-1} g p_{g_i} \tag{3}$$

at each image time i, where in our study there are $G = 4$ groups $g = 0$, 1, 2, and 3, and p_g is the diagnosed group probability. From C_p and C_o, the observed category at each image time i, several statistical metrics were determined for the image sequence. They are Brier Score

$$BS = \frac{1}{N(G-1)^2} \sum_{i=1}^{N} (C_{p_i} - C_{o_i})^2, \tag{4}$$

Bias

$$Bias = \frac{1}{N(G-1)} \sum_{i=1}^{N} (C_{p_i} - C_{o_i}) \tag{5}$$

and Diagnosis Uncertainty

$$DU = \frac{1}{N} \sum_{i=1}^{N} [1 - \max_g (p_{g_i})]. \tag{6}$$

In our study, N represents the number of image times in the respective image sequence. In addition, frequency distribution fit (FDF) defined by

$$FDF = \frac{1}{N_a} \sum_{g=0}^{G-1} \left| \frac{m_g}{n_g} - 1 \right| n_g \tag{7}$$

For all application set sequences (N_a), where m_g is the number of image times in which group g was the most likely category (greatest diagnosed probability), and n_g is the number of observed group g image times.

Method 1: After acquiring the ISOON Hα image sequences and partitioning them into the ISS as listed in Table 1 [27], we tried them out on the legacy flare probability diagnosis development and application algorithms from the previous study. Norquist and Balasubramaniam [26] refer to this version as the Hα Eigenvector Flare Categorization (HEFC) algorithms. In this report we will refer to it as the Image Time Flare Probability Diagnosis Method 1[26]

Method 2: A look at some preliminary results from the Method 1 algorithms (not shown) indicated some degree of overlap among the four groups. At many FLI 0 image times in an application sequence, one of the non-zero FLI categories was diagnosed with the largest probability. This was often due to none of the four categories having a probability exceeding 0.5, leading to an ambiguity in the designation of most likely flaring category. We felt that this suggested a need to achieve greater separation among the group means in discriminant space to get a more distinctive diagnosis of flare category probability.

In seeking greater discrimination among the flaring categories, we experimented with using alternative forms of the eigenvectors. We saw that the range of values for a specific eigenvector would vary from sequence to sequence. Since we were using multiple image sequences in the development algorithm, we sought a more uniform representation of the eigenvector information across sequences. To that end, we considered the use of the time rate of change of the eigenvectors instead of their actual value at each image time. Since the image cadence is one minute for the ISOON Hα images, we decided to examine the use of 1-minute eigenvector changes as the predictors.

We then applied a five-point smoother to the time series of each of the nine leading eigenvectors, then created a scatter plot of one-minute eigenvector changes against one-minute x-ray flux changes for each eigenvector of selected image sequences with FLI categories 0-3. The results of the analysis are shown in Figure 10 below.

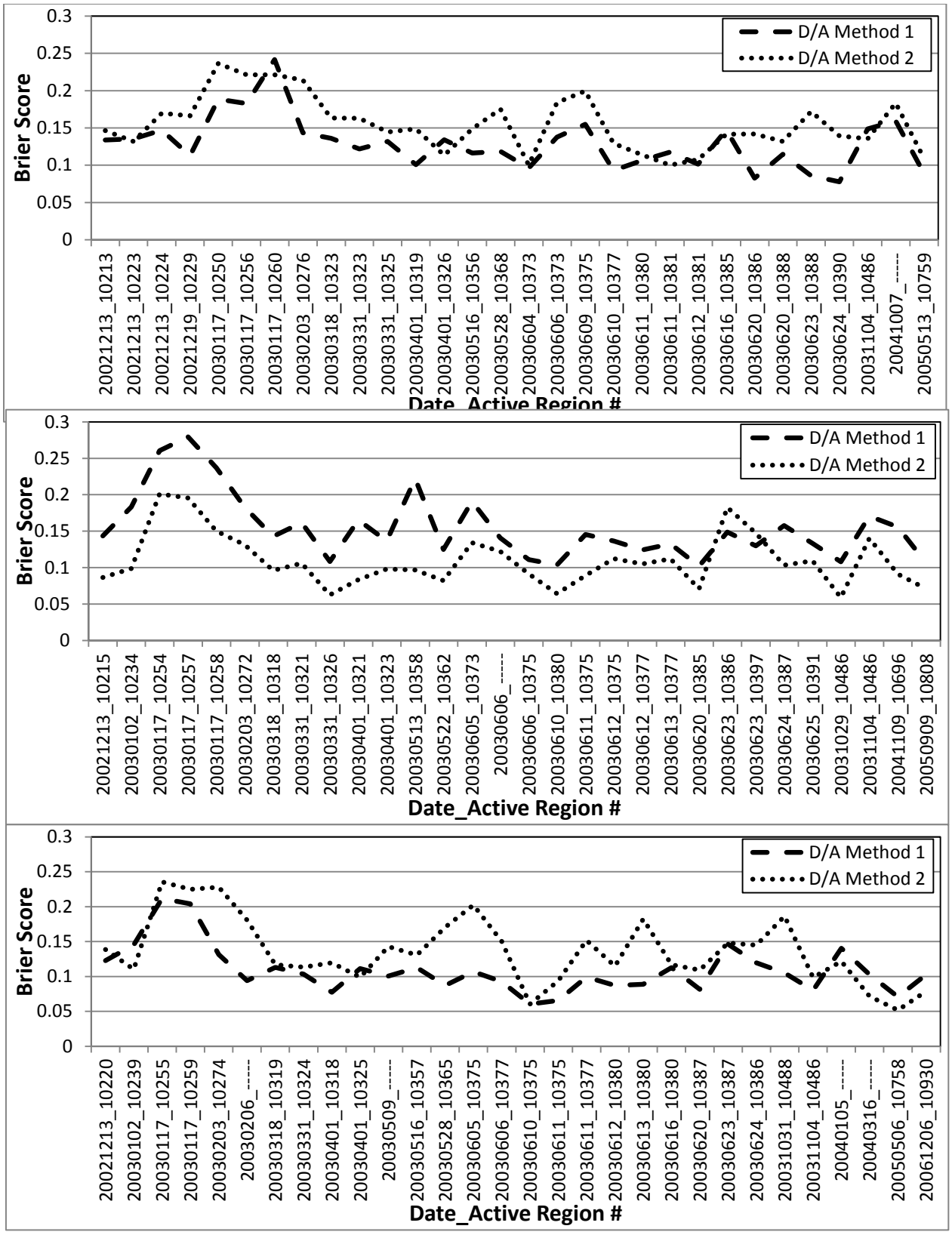

Figure 10. **Brier Skill Scores** Brier Score of Methods 1 and 2 for Application Sets (1), (2) and (3)

5. CONCLUSIONS

5.1. Sunspot Area Flare Statistics and Interpretation

- Sub-flares: 85% of sub-flares show a decrease in penumbral brightness. Interpretation: vanishing penumbra.
- B Flares: 100% of B flares show no reliable trends
- C Flares: 53% show increase in umbral area, 57% show an increase in umbral brightness and 75% show increasing penumbral brightness. Interpretation: C flares show an increase in sunspot area after flares. Magnetic fields spreads over a larger area – a weaker larger sunspot after flares
- M flares: 54% show decrease in umbral brightness while 63% show an increase in penumbral area. Interpretation: Redistribution of umbral magnetic fields into the inclined fields of the penumbra
- X flares: 60% show an increase in umbral area, 80% show a increase in umbral brightness, 60%show an decrease in penumbral area, 60% show an increase in penumbral brightness. Interpretation: Magnetic fields in umbra become weaker and their area become larger.

A trend better than 50% (0.5) shows the reliability of the measurement, for probabilistic use in flare prediction models.

5.2. SCBs

SCB preceede flare intensities, on the average by 12 minutes. The propagate away from flare kernels brightening about magnetic foot-points due to electron deposition and resulting chromospheric evaporation. SCBs occur duing the impulsive phase of flare. These are special case of chromospheric compact brightenings accompanying CMEs. The research work on SCBs provides us with a good heuristic model of CMEs accompanying solar flares, which are preceeded by SCBs, providing a good specification (nowcasting) of flare characteristics.

5.3. PCA Analysis

From PC components sorted from weak flares to strong flares, we find 2 distinct categories of flares (below C4 and above C8) separated by a transition region (C4-C8), with possibly two distinct underlying physical mechanisms From PC components correlated from one flare to another, we find low correlation between eigen vectors before the flare and high correlation after the flare.

- pre-flare: strong local correlation of similar strength flares
- post-flare energy release mechanism is similar regardless of flare strength

Hence, analysis of ISOON data indicates two distinct flare energy build-up mechanisms, one for weak flares and another for strong flares. Such a distinction should help us develop distinct model of flares, one for the low-energy flares, and the other for the high energy flares. Further research will be necessary to understand the intermediary stages of between C4.0 and C8.0 flares.

5.4. MVDA Analysis Of Flares

In addition to the statistical metrics computed for each image sequence as shown in Figures 10, we present their values determined from all image times over all sequences in each application set in Table 2

Table 2: Statistical Metrics for MVDA Analysis

	Application Set 1		Application Set 2		Application Set 3	
	Method 1	Method 2	Method 1	Method 2	Method 1	Method 2
Brier Score	0.12	0.15	0.15	0.10	0.10	0.13
Bias	0.31	0.35	0.35	0.27	0.28	0.31
DU	0.44	0.48	0.45	0.39	0.45	0.43
FDF	0.89	0.92	0.87	0.56	0.66	0.82

6. SUMMARY

Our original ultimate goal in this endeavor was to be able to predict flaring from the high-cadence ISOON data. Unfortunately, we were not able to achieve a high enough level of flare diagnosis skill to go beyond that level. We still feel that the apparent distinction among the flaring categories as evident in the Hα eigenvectors may have potential for useful short-term flare prediction. We feel the need to combine Hα image eigenvectors to Hα Doppler eigenvectors as well as magnetic field fluctuation eigen-vectors to further understand the influence of these methods. While Hα image analysis is by far the most promising exploitation for flare prediction, its effectiveness will improve with combining it with white-light/continuum measurements of changing sunspot (umbral and penumbral) areas, and Doppler measurements. A preliminary analysis of the Doppler PCA and MVDA analysis is mentioned in Norquist, D. C. and K. S. Balasubramaniam [27]. The Doppler data that we currently have does not cover all activity measurements shown in Table 1.

Our next step will be to understand eigen-vector measures from data measures in chromospheric (UV), vector magnetic and other wavelengths, using such data as the Solar Dynamics Observatories

REFERENCES

[1] Somov, B.V., *Physical Processes in Solar Flares*, Kluwer Academic Publishers, Dorcrectht, 1992.

[2] Svestka, Z., B. V. Jackson, and M. E. Machado, *Solar Flares*, Springer Verlag, Berlin, 1992.

[3] Balasubramaniam, K. S, S. L. Keil, and R. N. Smartt, *Solar Drivers of Terrestrial and Interplanetary Disturbance*, Astron. Soc. Pac. Conf. Ser., Volume 68, 1996.

[4] Bothmer, V. and I. A. Daglis, *Space Weather, Physics and Effects,* Springer Praxis, UK, 2007.

[5] McIntosh, P. S., *The classification of sunspot groups,* Sol. Phys., 125, pp. 251-267, 1994.

[6] Bornmann, P. L. and D. Shaw, *Flare rates and the MacIntosh active-region classifications,* Sol. Phys., 150, pp. 127-146, 1994.

[7] Gallagher, P.M., Y.-J. Moon, and H. Wang, A*ctive-Region Monitoring and Flare Forecasting I. Data Processing and First Results*, Sol. Phys., 209, pp. 171-183, 2002.

[8] Wheatland, M. S., *A Bayesian Approach to Solar Flare Prediction,* Astrophys. J., 609, pp. 1134-1139, 2004.

[9] Wheatland, M. S., *A statistical solar flare forecast method,* Space Weather, 3, S0700, 2005.

[10] Smith, J. B., Jr., et al., ASP Conf. Ser., Vol. 68, p. 55, 1996.

[11] Falconer, D., *A prospective method for predicting coronal mass ejections from vector magnetograms,* Journal of Geophysical Research, 106, p. 25,185, 2001.

[13] Barnes, G., K. D. Leka, E. A. Schumer, and D. J. Della-Rose, *Probabilistic forecasting of solar flares from vector magnetogram data,* Space Weather, *5,* S0900, 2007.

[12] Ambastha, A., M. J. Hagyard, and E. A. West, *Evolutionary and flare-associated magnetic shear variations observed in a complex, flare-productive active region,* Solar Phys., 148, p. 277, 1993.

[14] Georgoulis, M. and D. Rust, *Quantitative Forecasting of Major Solar Flares,* ApJ, 661, Letter 109, 20 May 2007.

[15] Smith, J. B., Jr., et al., *An Objective Test of Magnetic Shear as a Flare Predictor,* in Solar drivers of the interplanetary and terrestrial disturbances, ASP Conference Series, Eds: K. S. Balasubramaniam, Stephen L. Keil, and Raymond N. Smartt, Vol 95, p. 55, 1996.

[16] Neidig, D., et al., *The USAF Improved Solar Observing Optical Network (ISOON) and its Impact on Solar Synoptic Data Base,* in Synoptic Solar Physics, ASP Conference Series, Eds: K. S. Balasubramaniam, Jack Harvey, and D. Rabin, Vol. 140, p. 519, 1998.

[17] Contarino, L., et al., *Flare Forecasting Based on Sunspot-Groups Characteristics*, Acta Geophys, 57, p. 52, 2009.

[18] Balasubramaniam, K. S., A. A. Pevtsov, D. F. Neidig, E. W. Cliver, B. J. Thompson, C. A. Young, S. F. Martin, and A. Kiplinger, *Sequential Chromospheric Brightenings beneath a Transequatorial Halo Coronal Mass Ejection,* Astrophysical Journal, 630, pp. 1160-1167, 2005.

[19] Balasubramaniam, K. S., A. A. Pevtsov, D. F. Neidig, and R. A. Hock, *Large scale solar chromospheric eruptive activity-a signature of magnetic reconnection,* Eds: N.Gopalswamy and A. Bhattacharyya, Proceedings of the ILWS Workshop, 65, 2006.
http://www.physics.emory.edu/~weeks/idl/index.html, accessed June, 2009.

[20] Crocker, J.C. and E. R. Weeks, Particle Tracking in IDL,
http://www.physics.emory.edu/~weeks/idl/index.html, accessed June, 2009.

[21] Kirk, M. S., K. S. Balasubramaniam, J. Jackiewicz, R. T. J. McAteer, and R. O. Milligan, *Properties of Sequential Chromospheric Brightenings and Associated Flare Ribbons,* Astrophysical J. 750, p. 145, 2012.

[22] Kirk, M. S., K. S. Balasubramaniam, J. Jackiewicz, B. J. McNamara, and, R. T. J. McAteer, *An Automated Algorithm to Distinguish and Characterize Solar Flares and Associated Sequential Chromospheric Brightenings,* Solar Phys. 283, p. 97, 2013.

[23] Kirk, M. S., K. S. Balasubramaniam, J. Jackiewicz, B. J. McNamara, and R. T. J. McAteer, *Sequential Chomospheric Brightening: An Automated Approach to Extracting Physics from Ephemeral Brightening,* Astron. Soc. Pacific, Vol. 463, p. 267, 2012.

[24] Eydenberg, M., K. S. Balasubramaniam, and Ariste Lopez, *A. PCA-Interpolation Methods for Inversion of Solar Stokes Profiles. I. Inversion of Photospheric Profiles*, Astrophysical J. 619, p. 1167, 2005.

[25] Norquist, D. C., *An analysis of the sunspot groups and flares of Solar Cycle 23,* Solar Phys., 269, pp. 111-127, 2011.

[26] Norquist, D. C. and K. S. Balasubramaniam, *Diagnosis of Solar Flare Probability from Chromosphere Image Sequences,* AFRL-RV-PS-TP-2011-0005, Air Force Research Laboratory, Kirtland AFB, NM, Sep 2011.

[27] Norquist, D. C., and K. S. Balasubramaniam, *More Diagnosis of Solar Flare Probability from Chromosphere Image Sequences*, AFRL-RV-PS-TP-2012-0194, Air Force Research Laboratory, Kirtland AFB, NM, Sep 2012.

[28] Wilks, D. S., *Statistical Methods in the Atmospheric Sciences, Second Edition*, Academic Press, Burlington, MA, 2001.

DISTRIBUTION LIST

DTIC/OCP
8725 John J. Kingman Rd, Suite 0944
Ft Belvoir, VA 22060-6218 1 cy

AFRL/RVIL
Kirtland AFB, NM 87117-5776 2 cys

Official Record Copy
AFRL/RVBXS/Karatholuvu Balasubramaniam 1 cy